Semi-analytical modelling of prompt redeposition in a steady-state plasma

L Cappelli, N Fedorczak, E Serre

Semi-analytical modelling of prompt redeposition in a steady-state plasma

L. Cappelli*[1,2], N. Fedorczak[2], and E. Serre[1]

[1]M2P2 Aix-Marseille Univ, CNRS, Centrale Marseille, 13013, Marseille, France
[2]CEA, IRFM, F-13108, Saint-Paul-lez-Durance, France

Abstract

A steady-state, 1D semi-analytical model for prompt redeposition based on the separation between redeposition caused by the electric field in the sheath and redeposition related to gyromotion is here described. The model allows for the estimation of not only the fraction of promptly redeposited flux but also the energy and angular distribution of the non-promptly redeposited population, along with their average charge state. Thus, the temperature and mean parallel-to-B velocity of the non-promptly redeposited flux are also available. The semi-analytical model was validated against equivalent Monte Carlo simulations across a broad range of input parameters. In this paper the eroded material under exam was tungsten (W) for which the code demonstrated consistent agreement with respect to numerical results, within its defined validity limits. The model can theoretically provide a solution for any material, temperature and electron density profile in the sheath, monotonic potential drop profile, and sputtered particles energy and angular distribution at the wall. As such, this code emerges as a potential tool for addressing the boundary redeposition phenomenon in fluid impurity transport simulations.

Keywords— semi-analytical model, prompt-redeposition, tungsten, plasma-wall interactions

1 Introduction

In future tokamak reactor handling of power exhaust and erosion of walls pose a significant challenge. As power exhaust becomes increasingly significant, predilected plasma-facing materials have shifted towards heavy species like tungsten (W) because more adapt to withstand high heat fluxes and erosion [1]. However, the penetration of heavy ions into the core can result in unacceptable radiative losses, posing the risk of plasma destabilization and collapse [2]. The complex interplay between power exhaust, erosion, and plasma stability necessitates meticulous modeling for reactor design. Fluid multispecies solvers like SOLEDGE [3], [4] and SOLPS [5], enable the study of dynamic interactions between impurities and plasma ions, as well as the interplay between core contamination and radiated power. A variation in radiated power may affect plasma-wall interactions (PWIs), thus erosion. Understanding the feedback dynamics between PWIs and contamination becomes crucial in assessing the impact of contamination on plasma performance. Nevertheless, fluid impurity transport codes face limitations, being unable to resolve PWIs and transport in the plasma sheath. Indeed, to function correctly, impurity sources at the plasma-wall boundary of the fluid solver domain have to be provided. One way to do this, is by neglecting impurities' transport in the sheath assuming that their ionization mean free path is larger than the sheath width. Essentially, all eroded material is assumed to enter the simulation domain and contribute to the boundary source. In such cases, it suffices to integrate models capable of estimating the gross fluxes Γ_{gross} of eroded materials resulting from PWIs due to local plasma-wall conditions, such as

*Corresponding author: L. Cappelli, email: luca.cappelli@univ-amu.com

EIRENE [6]. Anyway, penetration of impurities in the fluid codes domain, especially if heavy, remains largely influenced by the prompt redeposition phenomenon which should be accounted to correctly assess boundary impurity sources [7]–[11]. Indeed, the fraction f_p of the eroded flux Γ_{gross} that promptly redeposits either does not penetrate the fluid domain or only passes through it temporarily without contaminating the plasma. Therefore, the more accurate boundary condition is the net inflow Γ_{net}, defined as $\Gamma_{net} = (1 - f_p)\Gamma_{gross}$. By definition, an eroded particle is promptly redeposited if it intersects a wall during the first Larmor period following its initial ionization, regardless of any possible reflections. For instance, if an eroded particle ionizes very close to the wall, in the plasma sheath, the probability that the particle's trajectory will intersect the wall recombining with it is significant. Models for f_p aim to incorporate prompt redeposition in fluid transport code boundary conditions as function of plasma quantities at the sheath entrance, i.e. at the boundary between the fluid domain and the plasma sheath. Unfortunately, a general solution remains elusive. Previous important attempts, based on analytical models or fits, exhibit indeed limited applicability [7], [9]. The difficulty in discovering a universally applicable solution for f_p and other essential parameters related to heavy-impurity transport, including charge state and temperature, has led to alternative approaches where PWIs are treated employing kinetic Monte Carlo codes such as ERO2.0 [12] and GITR [13]. These models kinetically solve the transport of eroded ions in the sheath and plasma edge in real geometry. They also need to be coupled to a fluid plasma solver to get a static plasma background in which impurities are kinetically transported. The main downsides of this approach are the computational costs and convergence times associated with Monte Carlo calculations. Furthermore, the fixed plasma background provided by fluid solvers does not evolve in time, not allowing the study of temporal plasma evolution concerning contamination and radiated power. In this paper, we propose a semi-analytical model to calculate the net flux Γ_{net} and other relevant quantities. This includes the non-prompt redeposited fraction $(1-f_p)$, the net flux temperature, average charge state, and mean parallel velocity to the magnetic field, for a broad range of plasma conditions at the sheath entrance. This model holds potential for accurately computing boundary conditions for fluid multispecies transport solvers.

2 Model description

This section discusses the fundamental assumptions, geometry, and workflow associated with the semi-analytical model and how it will be employed in this work. The code solves prompt redeposition of eroded particles in the sheath in a well-defined physical framework.

2.1 Physical framework

Consider the erosion of a flat wall extending along the plane $z = 0$ and exposed to a uniform magnetic field $\vec{B}$ as illustrated in figure 1a. Along the z-axis above the wall, the Debye sheath and the Chodura sheath develop. In this paper, the combination of Debye plus Chodura sheaths will be referred to simply as 'sheath'. The sheath is considered uniform with respect to the xy coordinates and ion-ion collisions are neglected. Its entrance coincides with the condition of plasma average parallel-to-B velocity equal to the sound speed.

Impinging ions strikes the surface with energy E_0 and angle $\alpha = arctan\left(\sqrt{v_x^2 + v_y^2}/v_z\right)$ while eroded particles trajectories are identified within a spherical coordinate system, where the azimuth angle is ϕ and the poloidal one is θ, as reported in figure 1b.

Since the subject is prompt redeposition, the sheath, incident ion flux, and composition of the eroded material are assumed to be in a steady state over a Larmor period of the eroded species (referred to as T_L), during which plasma fluctuations are disregarded.

2.2 Model workflow

As illustrated in figure 2 the model takes as input: the Sputtered energy and Angular Distribution (SEAD) related to Γ_{gross}, the one-dimensional profiles along z of electronic density and temperature $(n_e(z), T_e(z))$, the potential drop $V(z)$, the magnetic field, and atomic data for the ionization rate coefficients (denoted as S), where only ionization by electron collisions are considered. The SEAD represents the probability that a fraction of the gross flux is populated by particles having energy in the interval $E, E + dE$ and direction in the solid angle $\Omega, \Omega + d\Omega$. In the following model, the SEAD is calculated as done in [11]. Therefore, it depends on the incident ion mass, charge and angle of incidence (α). It also depends on the assumed velocity distribution at the sheath entrance for the impinging flux. For this particular application, the comparison was made assuming that the average angle of incidence $\overline{\alpha} = 40$ deg, a gamma function for the parallel velocity distribution and a

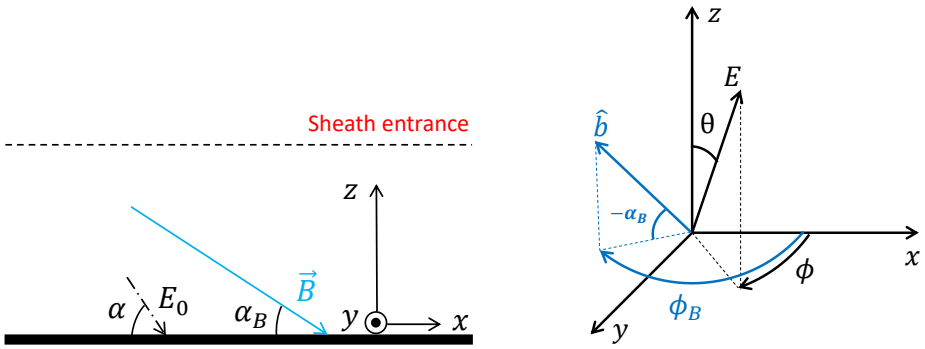

Figure 1: a) Coordinate system aligned with a planar surface, where $\phi_B = 0$ (see right image). The energy and angle of an incoming ion are represented as E_0 and α, while $\vec{B}$ is the magnetic field vector. b) Representation of angles identifying both the initial direction of a sputtered particle with energy E and the direction of the magnetic field $\hat{b}$.

maxwellian distribution for the perpendicular velocity distribution. Once the energy and angular distribution of the incident flux (IEAD) is known, the energy distribution of the eroded particles is calculated as given in equation (2). That is, it is equal to the integral between a normalized Thompson function ($f_{th}(E_0, E, \theta)$) taken from [14], the sputtering yield y and the IEAD. The sputtering yield of W was taken from [15].

$$SEAD(E) = \frac{\int IEAD(E_0, \overline{\alpha}), y(E_0, \overline{\alpha}) f_{th}(E_0, E, \theta) dE_0}{\int \left(\int IEAD(E_0, \overline{\alpha}), y(E_0, \overline{\alpha}) f_{th}(E_0, E, \theta) dE_0 \right) dE} \tag{1}$$

As for the angular distribution, this is considered cosinusoidal with respect to the poloidal angle (θ) and uniform with respect to the azimuth ϕ. Since a spherical coordinate system is used, the SEAD depends on the energy E and the solid angle $\Omega = sin(\theta) d\theta d\phi$. The resulting SEAD distribution expressed as a function of energy and poloidal angle is given in equation (2):

$$SEAD(E, \theta, \phi) = \frac{1}{2\pi} SEAD(E) sin(2\theta) d\theta d\phi \tag{2}$$

Concerning the electron profiles along the z-axis, the density profile in the sheath is approximated using the Boltzmann factor:

$$n_e(z) = n_e^{SE} exp(-V(z)/T_e(z)) \tag{3}$$

Here, n_e^{SE} represents the electron density at the sheath entrance, respectively, while V denotes the electric potential within the sheath. The chosen potential profile is taken from [16]. It is characterized by a parameter k that is directly proportional to the sheath width as defined in the same reference. Results shown in section 6 are all evaluated setting $k = 2$ and assuming uniform temperature profiles, specifically the temperature is set equal to its value at the sheath entrance, i.e. $T_e(z) = T_e^{SE}$. Finally, eroded particles' ionization rate coefficients $S(n_e, T_e)$ are taken from ADAS [17]. These coefficients account only for ionization caused by electron collisions, with no consideration of recombination processes.

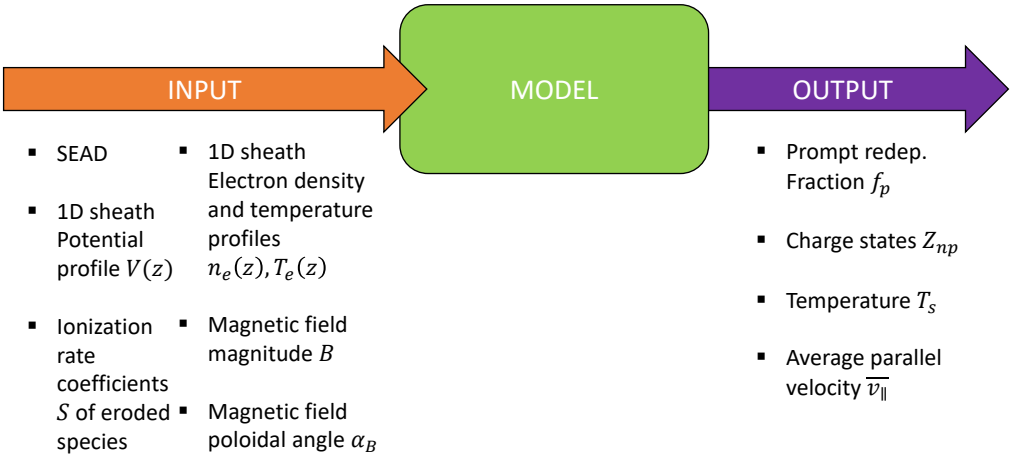

Figure 2: Workflow scheme: the model processes estimates of the fraction f_p, charge state (denoted as Z_{np}), and other fluid quantities of the non-promptly redeposited population based on 1D profiles of electron density, temperature, potential drop, SEAD, atomic ionization data, and magnetic configuration.

The model not only estimates the fraction f_p but also provides values for other properties of the $1 - f_p$ fraction, referred to as NP (non-prompt). As shown in Figure 2, in addition to f_p, the model outputs include the NP distribution of charge states, the NP temperature (also called source temperature, T_s), and the average NP parallel-to-B velocity, denoted as $\overline{v_\parallel}$.

3 Redeposition Dynamics

In the physical framework described in section 2.1 prompt redeposition is caused by three different dynamics. The first one is linked to an energetic balance as discussed in section 3.1.1. Specifically, a fraction (denoted as f_R^E) of the gross flux is populated by particles undergoing ionization inside the sheath in a potential well larger than their initial energy, thus they don't have enough energy to escape and they are redeposited. Another way a sputtered ion may redeposit is related to its gyromotion, see section 3.1.2. Indeed, even if a sputtered particle ionizes outside the sheath, it still may redeposit because of its trajectory as depicted in figure 5. The fraction of Γ_{gross} redepositing because of gyromotion is here denoted as f_R^G. Ultimately, a portion f_R^{GE} of Γ_{gross} ionize sufficiently far from the wall to surpass the sheath electric potential, yet it experiences significant deflection by it.

3.1 Two-groups model

A simplification of the redeposition mechanisms is proposed here, referred to as the Two-groups model. In this model, the fraction f_R^{GE} is incorporated into f_R^G, with the assumption that the influence of deflection caused by the electric field on the non-promptly redeposited (NP) fraction is negligible. Consequently, the velocity components perpendicular and parallel to the magnetic field of an eroded particle are considered conserved at their respective initial values. This setup allows for a direct association between the redeposition probability and the SEAD at the wall. The main assumption of the two groups model is to assume that the energy of the fraction $1 - f_R^E$ is approximately unaffected by the further deceleration due to the remaining potential barrier. As it will be shown in the results section 6, this model breaks when the ionization distance becomes so short that most eroded particles will ionize in the sheath and are consequently deflected and decelerated.

3.1.1 Enegetic redeposition

To begin, let us study the ionization of a neutral particle with velocity vector $\vec{v}$ immersed in a plasma. For a static plasma, its ionization mean free path λ is equal to the ratio of its velocity module (v) to the ionization frequency. In case of electron-ionization the ionization frequency is equal to the product between the ionization

rate coefficient S and the electron density profile: $\omega_{ion} = n_e S(n_e, T_e)$. Therefore, ω_{ion} depends on plasma electron temperature and density.

$$\lambda = \frac{v}{\omega_{ion}} \tag{4}$$

Unless λ is relatively small, a neutral particle encounters variable density and temperature conditions during its path before ionization. If the particle follows a path identified by the coordinate z, its instantenous probability to ionize in $dt = dz/v_z$ is given by:

$$\frac{\omega_{ion}(z)}{v_z} dz$$

Where v_z is the velocity along the z-axis as shown in figure 1. Consider a neutral particle emitted from a planar surface situated in $z = 0$. By definition, its average probability to ionize is unitary when the particle reaches its mean free path λ_z.

$$\int_0^{\lambda_z} \frac{\omega_{ion}(z)}{v_z} dz = 1$$

Therefore, the velocity v_z required to ionize on average at a perpendicular distance λ_z is equal to the integral of the ionization frequency ω_{ion} along z, as reported

$$v_z = \int_0^{\lambda_z} \omega_{ion} dz \tag{5}$$

The inverse of equation (5) gives the mean free path as function of the velocity along the z-axis, called $\lambda_z(v_z)$.

The mean free path λ_z, is equivalent to the first moment of the ionization probability density function (PDF) along the z-axis for a neutral particle with a given initial velocity $\vec{v}$, as defined in equation (7). Assuming a flat and uniform sheath along the xy plane implies that the ionization PDF, represented as $f(z|E, \theta)$, depends solely on the particle's initial energy and poloidal angle. The ionization probability within the interval z to $z + dz$ is determined by the product of the probability of not ionizing up to z times the probability of ionizing within the interval z to $z + dz$. The probability a neutral has to not ionize up to a distance z as reported in [11] is equal to:

$$e^{-\frac{1}{v_z}\int_0^z \omega_{ion} dz'}$$

where it is derived through a simple static 1D Vlasov equation. Consequently, the ionization distribution can be expressed as shown in equation 6:

$$f(z|E, \theta)dz = \frac{\omega_{ion}}{v_z} e^{-\frac{1}{v_z}\int_0^z \omega_{ion} dz'} dz \tag{6}$$

As anticipated, the first moment of the ionization distribution $f(z|E, \theta)$ is equal to λ_z (see equation (7)), which is also equal to the inverse of equation (5).

$$\int_0^{\infty} f(z|E, \theta) z dz = \lambda_z \tag{7}$$

The mathematical derivation to prove that equations (7) and the inverse of (5) are equivalent, to date was not found. The challenge resides in analytically solving the integral of ω_{ion}, since it is implicitly a function of the electron density decay n_e (see equation (3)), hence in this case, of the Boltzmann factor. Anyway, the equivalence was proved numerically comparing both the inverse of equation(5) and equation (7) with Monte Carlo results, see figure 3. It is worth noting that in figure 3, the numerical estimation of the mean free path deviates from the analytical one as the energy $E_z = Ecos(\theta)^2$ along the z-axis increases. This discrepancy is attributed to the lower number of particles populating the high-energy tail, resulting in insufficient sampling for $E_z > 30$ eV, leading to a poor statistical representation.

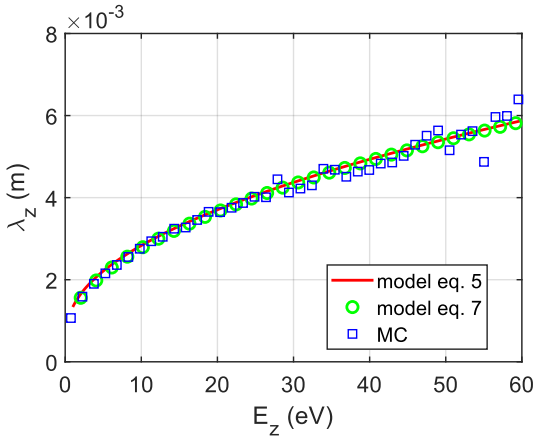

Figure 3: Bombardment of N^{+5} with W. Comparison of analytical (red line refers to the inverse of equation (5), while green circles refer to equation (7)) and Monte Carlo (MC) results for the average ionization length λ_z as function of the initial kinetic energy of neutral sputtered W atom along the z-axis. MC estimates are less accurate for higher energies since it is hard to analogically sample the tails of the sputtered distribution. The plasma background for this figure is characterized by a $n_e = 5e18$ m^{-3}, $T_e = T_i = 20$ eV, $B = 3$ T, and $\alpha_B = 4$ deg.

Once the ionization distance of a neutral particle is determined, it also establishes the force that the electric field will exert on it after ionization. In a scenario where the electric potential V transitions from zero at the sheath entrance to negative within the sheath, ionized particles within this region can surpass the electric potential barrier only if their initial kinetic energy along the positive z-direction exceeds the potential drop at the ionization position (expressed as $E_z > -V(z)$). This principle strictly applies in non-magnetized plasma conditions. In reality, the presence of gyromotion introduces complexity. The xy components of the initial kinetic energy contribute to the likelihood a particle ionized at a distance z has to overcome the potential corresponding potential drop $V(z)$. In this model it is assumed that particles respecting the relation $E_z > -V(z)$ will be poorly magnetized because of the dominance of the electric field force influencing their motion. Under this assumption, if particles undergo ionization in a potential well greater than their initial kinetic energy E_z, they are considered redeposited. If the electric potential within the sheath monotonically decreases a unique ionization distance (denoted as z^{*E}) can be identified as the threshold ionization distance below which a particle with initial kinetic energy E_z will redeposit. The length z^{*E} serves as a distinguishing factor between particles with ionization distance $z \leq z^{*E}$, which will be considered re-deposited due to the electric field, and particles with ionization distance $z > z^{*E}$, which overcome the electric field and may have a chance to contaminate the plasma. Once the SEAD is known, it is possible to calculate the fraction of Γ_{gross}, denoted as f_R^E, redeposited because of the electric field force, as shown in equation (8).

$$f_R^E = \int SEAD(E,\theta) \left(\int_0^{z^{*E}(E,\theta)} f(z|E,\theta)dz \right) dEd\theta \tag{8}$$

To determine the threshold distance z^{*E}, the potential V must be inverted to locate the point where it is equal to the initial energy along the z-axis: $E_z = Ecos(\theta)^2 = -V(z^{*E})$. Following the same line of reasoning the threshold distance z^{*E} can also be used to calculate the SEAD populated by particles overcoming the electric field, as shown in equation (10). The fraction $1 - f_R^E$ ionizing far enough (i.e. with ionization distance $z > z^{*E}$) is denoted as NE.

$$f^{NE} = SEAD(E,\theta) \left(\int_{z^{*E}(E,\theta)}^{\infty} f(z|E,\theta)dz \right) \tag{9}$$

$$SEAD^{NE} = f^{NE} \Big/ \int f^{NE} dEd\theta \tag{10}$$

An important parameter is the electrostatic threshold distance λ_z^{*E} of the sputtered population. It is identified by reversing the total energy balance function (denoted as h) at zero, see equation (11). As the threshold distance z^{*E}, also λ_z^{*E} is a distinguishing threshold between particles whose mean free path $\lambda_z > \lambda_z^{*E}$ who on average will surpass the sheath electric potential, and vice versa. This parameter will be used in section 6 to normalize the dimensionless parameter $\hat{\lambda}$ (equation (33)).

$$h \equiv \frac{1}{2} m \left(\int_0^{\lambda_z} \omega_{ion} dz \right)^2 + V(\lambda_z) \tag{11}$$

$$\lambda_z^{*E} = h^{-1}(0) \tag{12}$$

The first moment of the ionization distribution $f(z|E,\theta)$ could provide a more computationally efficient way to estimate f_R^E compared to the calculations required by equation (8). This is accomplished by checking whether the mean free path of a sputtered particle is larger or smaller than λ_z^{*E}. A particle has a mean free path equal to λ_z^{*E} if its energy along the z-axis $E_z = -V(\lambda_z^{*E})$. That is, the energy of particles whose $\lambda_z = \lambda_z^{*E}$, denoted as E_m can be written as reported in equation (3.1.1). This represents the lowest mean energy required for a particle to overcome on average the potential drop.

$$E_m(\theta) \equiv \begin{cases} \frac{-V(\lambda_z^{*E})}{cos^2(\theta)}, & \text{if } V(\lambda_z^{*E}) < 0 \\ 0, & \text{otherwise} \end{cases}$$

An approximation of f_R^E is now computable if the SEAD at the wall is known, as reported in equation (13).

$$f_R^E \approx \int \int_0^{E_m} SEAD(E,\Omega) dE d\Omega \tag{13}$$

In figure 4a, $1 - f_R^E$ is depicted as function of the normalized mean average ionization length $\overline{\lambda_z}$ of W for a given SEAD, normalized by the distance λ_z^{*E}. If $\overline{\lambda_z} < \lambda_z^{*E}$, $1 - f_R^E$ falls rapidly and the difference between the full kinetic calculation with respect to the first moment approximation decreases. Figures 4a and 4b were obtained calculating the f_R^E associated with a population of neutral W particles sputtered by an incident flux of nitrogen ions (N^{+5}) while varying the electron density at the sheath entrance. Figure 4b shows the same data points but in relation to the electron density.

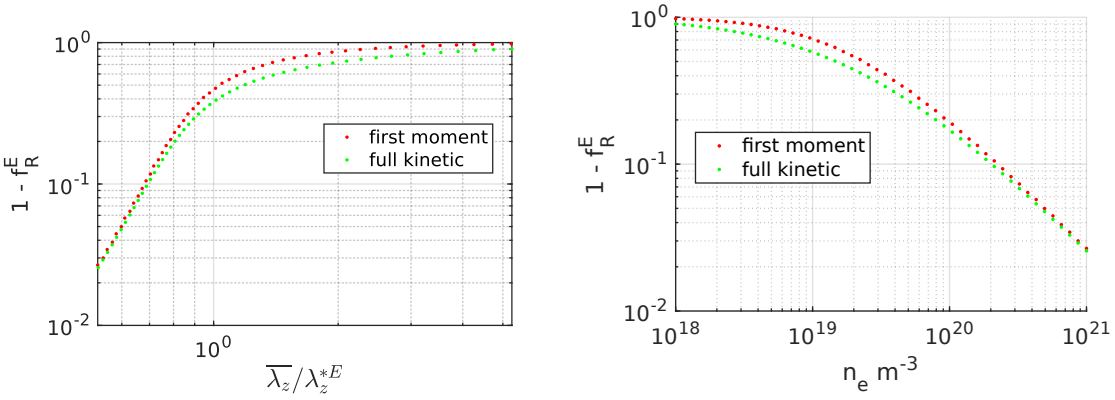

Figure 4: Fraction of W gross flux overcoming the sheath potential according to equations (8) (full kinetic) and (13) (first moment). Depicted results refer to the sputtering of W due to a flux of nitrogen ions (N^{+5}) with a variable electron density at the sheath entrance. All other parameters were fixed: $T_e = T_i = 20$ eV, $B = 3.7$ T, and $\alpha_B = 4$ deg.

The first moment approximation could be used in every way as the full kinetic approach. Indeed, there is even a first moment approximation of the SEAD^{NE}, see equations (14) and (16). The angular distribution of

the $1 - f_R^E$ fraction is approximated multiplying the angular distribution at the wall by the mean probability that a sputtered particle with a given poloidal angle θ will undergo energy-driven redeposition.

$$SEAD^{NE}(\theta) \approx \frac{SEAD(\theta)\left(1 - \int_0^{E_m(\theta)} SEAD(E)dE\right)}{\int_0^{\pi/2} SEAD(\theta)\left(1 - \int_0^{E_m(\theta)} SEAD(E)dE\right)d\theta} \tag{14}$$

The energy distribution is derived by eliminating the fraction of particles with energy lower than the minimum energy E_m. Therefore, the energy distribution function of particles not subject to electrical redeposition can be approximated as shown in equation (16).

$$SEAD^{NE}(E|\theta) \approx \int \frac{SEAD(E)H(E - E_m(\theta))}{1 - \int_0^{E_m(\theta)} SEAD(E,\theta)dE}d\theta \tag{15}$$

$$SEAD^{NE}(E) \approx \int SEAD^{NE}(E|\theta)SEAD^{NE}(\theta)d\theta \tag{16}$$

In this paper the first moment approximation is not utilized. When mentioning the model solution, it exclusively refers to the kinetic solution. Anyway the first moment approximation could be used in the future as a tool to reduce calculation time.

3.1.2 Geometric redeposition

As anticipated in the previous section, the fraction $1 - f_R^E$ not energetically redeposited could still redeposit. A particle ionized at a distance greater than its z^{*E} can redeposit because of its gyromotion bringing it back to the wall, or due to a combination between gyromotion and electric field force. The corresponding redeposited fractions are here denoted as f_R^G and f_R^{GE}, respectively. As demonstrated in prior studies [7] the redeposited fraction f_R^G primarily depends on the parameter $p = \lambda/\rho_{L^{+1}} = \omega_L/\omega_{ion}$. This parameter represents the ratio between the ionization length of the neutrally sputtered particles to their first-ionization Larmor radius, and it is independent of the sputtered particle initial energy. According to this model the parallel-to-B velocity is zero and redeposition is also independent of the magnetic field direction, which is considered parallel to the surface. Ultimately, the possibility an eroded ion has to undergo multiple ionization is disregarded. In figure 5 is depicted the geometrical redeposition according to this simplified model. Such approximation is not acceptable, especially for the erosion and redeposition of heavy ions. In this section, a more general model is proposed with the aim of relaxing most of the assumptions made in [7].

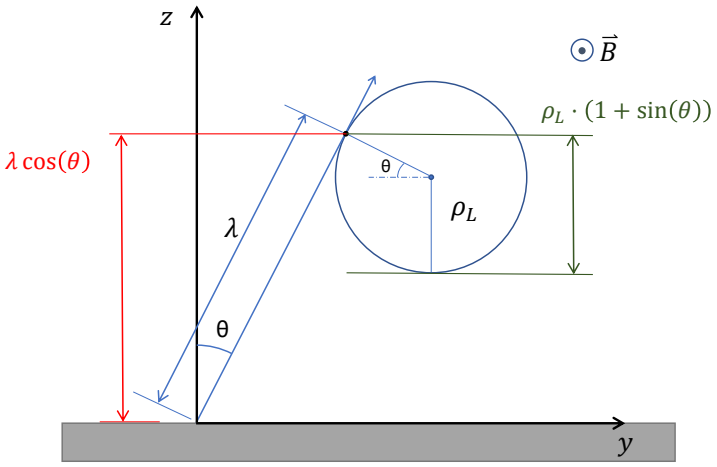

Figure 5: Possible gyromotion-driven redeposition along the yz plane for a particle emitted with poloidal angle θ and ionizing at a distance λ. In the absence of other forces, the particle can still redeposit because of gyromotion as suggested in [7]. The illustrated gyro-orbit is possible only in the absence of multiple ionization, external forces and for a magnetic field parallel to the eroded surface.

3.1.3 Model for geometric redeposition

The Larmor radius ρ_L of an eroded particle is proportional to the magnitude of its perpendicular-to-B velocity denoted as $|v_\perp|$. If the deflection caused by the electric field is negligible and in the absence of collisions $|v_\perp|$ is conserved. The magnitude $|v_\perp|$ of not redeposited particles can thus be expressed as a function of the initial direction of the particle, identified by the pair of angles (θ, ϕ), and of the poloidal magnetic field angle α_B. Equation (17) shows the squared ratio of the perpendicular velocity to the total magnitude, denoted as v.

$$\left(\frac{|v_\perp|}{v}\right)^2 = (\sin(\alpha_B)\sin(\theta)\cos(\phi))^2 + (\cos(\alpha_B)\cos(\theta))^2 + \frac{1}{2}\sin(2\alpha_B)\sin(2\theta)\cos(\phi) + (\sin(\theta)\sin(\phi))^2 \quad (17)$$

Besides perpendicular velocity, the radius ρ_L also depends on the charge state. In general, the Larmor radius of an ion with charge Z is equal to what stated in equation (18).

$$\rho_L = \frac{|v_\perp|}{Z\omega_L} \quad (18)$$

For simplicity, the Larmor radius is approximated using the average charge state of the $1 - f_R^E$ fraction reported in equation (26).

Similar to the model of [7] and to what reported in section 3.1.1, an eroded particle is assumed to redeposit during its gyromotion, if the projection along z of its first ionization length (i.e. $\lambda cos(\theta)$, see figure 5) is less than or equal to a certain threshold distance from the wall, here denoted as z^{*G}. While in [7] the threshold distance z^{*G} is equal to $(1 + sin(\theta))\rho_{L^{+1}}$, in this model it is also a function of the eroded particle's initial parallel-to-B velocity and its kinetic energy, since parallel transport and the possibility to re-enter into the sheath during the first gyromotion are both considered.
Ionized particles move closer or farther away from the wall depending on their $v_\parallel$ direction. In a time interval T_L, a particle with velocity $v_\parallel$ travels a distance $d = v_\parallel T_L$ along B if it does not redeposit. The projection of d on the z-axis is shown in equation (19):

$$d_z = v_\parallel T_L sin(\alpha_B) \quad (19)$$

As particles rotate, they can fall back into the sheath, where a well of electric potential draws them toward the wall. To include this dynamic, distance a is introduced, that is, the distance from the wall where the electric field potential V is equal to the total energy E of the moving particle. As stated in the equation (20), the distance a is obtained by inverting the function of the electric potential. If the energy of the particle E exceeds the total potential drop, then $a = 0$.

$$a = V^{-1}(-E) \quad (20)$$

In practice, the redeposition probability associated with the return of ions into the sheath is not accurately captured by the parameter a. A more precise solution would involve solving the complete trajectory, accounting for both the Lorentz and electric field forces. Equation (20), along with later equation (22), partially simulate the redeposition influenced by both gyromotion and the electric field, but these expressions are not physically accurate. Finally, in equation 21, the threshold ionization distance along the z-axis for gyromotion-related redeposition is provided.

$$z^{*G} = \rho_L\left(1 + \sin(\theta)\left[1 - 2H(\phi - \pi)\right]\right) cos(\alpha_B) + d_z\xi^5 + a \quad (21)$$

Here, H represents the Heaviside function while ξ is introduced to simulate the additional slowing and deflection of the $1 - f_R^E$ fraction due on average to the potential $V(\lambda_z^{*E})$ at the electrostatic threshold distance, as indicated in equation (22). The selection of ξ in equation (21) results from a tuning process aimed at achieving better agreement with the numerical results presented in section 6. As ξ approaches zero, the model assumptions become invalid, and other physical phenomena, such as drifts $\vec{E} \times \vec{B}$ between electric and magnetic fields, come into play.

$$\xi = 1 - \frac{\int E\ SEAD(E)^{NE} dE}{-V(\lambda_z^{*E})} \quad (22)$$

The equation (21) is valid for $\phi_B = 0$ and can be extended to the case $\phi_B = \pi$ by reversing the sign in front of the function $sin(\theta)$. Analogously to equation (8), we report in equation (23) the probability f_R^G of redepositing as a function of the energy E and initial direction (θ, ϕ). The redeposited fraction f_R^G is obtained by integrating along the z-axis from zero to the threshold values z^{*G} the ionization probability, as illustrated in equation (6).

$$f_R^G = \int SEAD(E,\theta,\phi) \left(\int_0^{z^{*G}(E,\theta,\phi)} f(z|E,\theta) dz \right) dE d\theta d\phi \tag{23}$$

4 Multiple ionization

When considering redeposition related to the gyromotion of ions, it is crucial to account for multiple ionization, as the Larmor radius depends on the ion charge. This section introduces an approximate model to estimate the average charge of ions populating the net flux, without tracking particles' trajectories. The model is based on the assumptions that sputtered particles populating the $1 - f_p$ fraction are those ionizing closer to the sheath entrance, where the Boltzmann factor is close to unity and the electron density and temperature are roughly constant. Hence, escaping particles can be viewed as traveling in a homogeneous medium, and their transport does not need to be solved. In the limit of coronal equilibrium, where recombination is disregarded and only electron ionization is considered, the time evolution of each ionization state of the $1 - f_p$ population can be described by a series of first-order differential equations, as follows.

$$\begin{cases} \psi_1 = e^{-\omega_{ion_1} t} \\ \partial_t \psi_i = -\psi_i \omega_{ion_i} + \psi_{i-1} \omega_{ion_{i-1}}, \quad \text{if i} > 1 \end{cases} \tag{24}$$

Here, $\psi_i(t)$ represents the fraction of particles in the i-th ionization state at time t, and ω_{ion_i} are the transition frequency from ionization state i to state i+1. The ω_{ion_i} terms are calculated assuming all plasma being at the sheath entrance condition (e.g. $n_e = n_e^{SE}$) during the whole Larmor period. At $t = 0$ all particles are in their first ionization state ($\psi_1 = 1$ and $\psi_{i>1} = 0$). The time evolution of the average ionization state is then expressed as the summation of the population fractions ψ_i multiplied by their corresponding ionization states, see equation (25).

$$\overline{Z}(t) = \sum_i \psi_i i \tag{25}$$

Assuming a uniform background proved to be a good approximation for the average charge of the non prompt fraction $1 - f_p$ (see figure 6), called $\overline{Z_{np}}$ and being equal to $\overline{Z}$ at $t = T_L$. However, such approximation is not perfectly suited to get the average ionization of the $1 - f_R^E$ fraction. In reality, particles that do not electrically redeposit can still travel partially inside the sheath where the density and temperature of electrons are lower. Additionally, redeposited particles are absorbed and have less time to undergo multiple ionization events. This is why the average ionization of the $1 - f_R^E$ population is expressed in equation (26) as an average between the charge of the non-prompt population and the charge state ($Z = 1$) of the electrically redeposited f_R^E fraction.

$$\overline{Z_{ne}} \approx f_R^E + (1 - f_R^E)\overline{Z_{np}} \tag{26}$$

The approximation for $\overline{Z_{np}}$ was tested for a wide range of electron temperature, density and magnetic field vector showing a good agreement in almost all cases, see figure 6.

5 Prompt redeposition

Once the threshold redeposition distances z^{*E} and z^{*G} are known, the probability a particle has to promptly redeposit is obtained through the integration from zero to the maximum between these two threshold distances of the ionization probability function along the z-axis. Accordingly, the f_p fraction is determined by the integral presented in equation (27).

$$f_p = \int SEAD(E,\theta,\phi) \int_0^{max\left(z^{*E}, z^{*G}\right)} f(z|E,\theta) dz dE d\theta d\phi \tag{27}$$

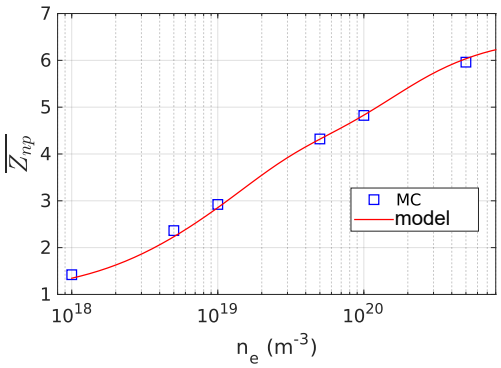

(a) $T_e = 20$ eV, $B = 3$ T, $\alpha_B = 4$ deg

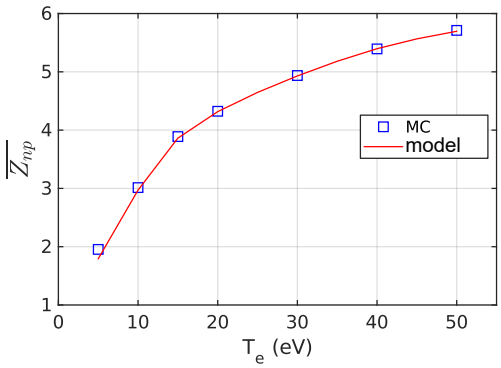

(b) $n_e = 5e19$ m^{-3}, $B = 3$ T, $\alpha_B = 4$ deg

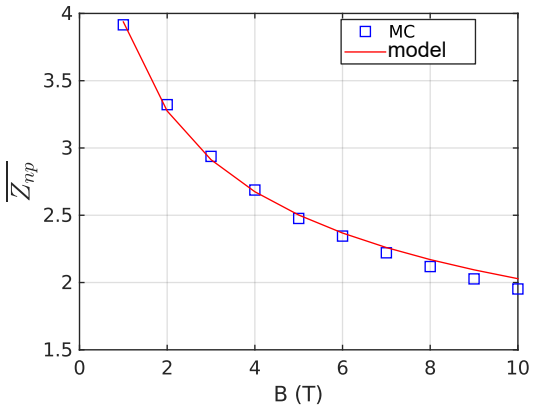

(c) $n_e = 1e19$ m^{-3}, $T_e = 20$ eV, $\alpha_B = 4$ deg

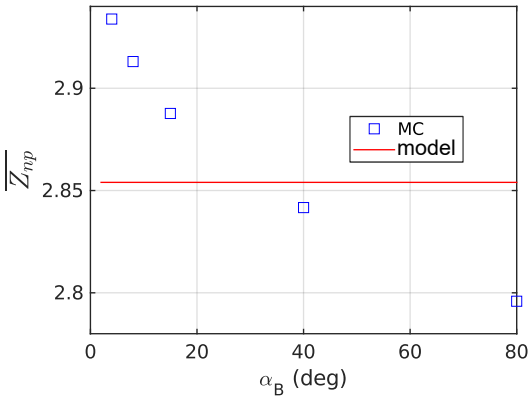

(d) $n_e = 1e19$ m^{-3}, $T_e = 20$ eV, $B = 3$ T

Figure 6: Average ionization state $\overline{Z_{np}}$ of W net flux. Comparison between the simplified model (red line) proposed in section 4 and Monte Carlo results (blue squares).

The integral from zero to the maximum between the two threshold distances of the ionization probability function along the z-axis can also be used to calculate an approximation of the SEAD for the NP fraction, as given in equations (28) and (29).

$$f^{NP} = SEAD(E,\theta,\phi)\left(1 - \int_0^{max\left(z^{*E},z^{*G}\right)} f(z|E,\theta)dz\right) \tag{28}$$

$$SEAD^{NP} = f^{NP} \Big/ \int f^{NP} dE d\theta d\phi \tag{29}$$

The energy distribution SEAD^{NP}(E) can be employed to derive the NP temperature, also referred to as the source temperature (T_s). This temperature is equivalent to two-thirds of the average energy of the NP fraction: $T_s = \frac{2}{3}\overline{E}_{NP}$ if energy is conserved from the ionization up to the end of the first gyration. In the absence of an additional energetic filter, T_s is approximately equal to the temperature of the non-prompt population, making it suitable for representing the temperature of the impurity source.

6 Results for Tungsten

The two-group model is applied to the case of a wall composed entirely of tungsten (W). A comparison is made between the outcomes of the analytical model and the numerical results obtained from Monte Carlo

(MC) simulations, considering identical wall geometry and input parameters. Refer to figures 1a and 2 for visual representations. The MC model is the same one employed in the article [11] where it was benchmarked against other local impurity transport codes such as ERO [18]. The fraction f_p is computed using equation (27). Where the threshold distance z^{*G} in equation (21) is determined using the mean Larmor radius $\overline{Z_{ne}}$ of the $1 - f_R^E$ fraction, as defined in equation (26).

$$\rho_L = \frac{|v_\perp|}{\overline{Z_{ne}}\omega_L}$$

The analytical model outputs are systematically compared with corresponding numerical results across a broad spectrum of input parameters. Importantly, the analytical model can be extended to account for other eroded species beyond W. In general, lighter eroded species tend to have longer first ionization lengths, bringing the analytical model closer to its ideal operating range. In fact, as the mean free path of first ionization decreases, the conservation of energy and parallel velocity during motion are compromised, as particles ionize in a potential well that is non-negligible compared to their initial kinetic energy, leading to major deflection, deceleration, and the appearance of $\vec{E} \times \vec{B}$ drifts. Finally, since fewer particles avoid redeposition model errors become more pronounced compared to the expected output. Tungsten is selected not only due to its significance in current reactor applications [1], but also because it represents a robust test case that challenges the model to its limits.

Results concerning the non-promptly redeposited W population in both MC and the two-group model are compared as listed below. In section 6.1, a comparison of the SEAD is shown, in section 6.2 the source temperature T_s of W is discussed, in section 6.3 the average parallel-to-B velocity is given as a function of the magnetic angle α_B. Finally, in sections 6.4 and 6.5, the prompt fraction f_p trends are calculated both for a fixed incidence angle $\alpha_B = 4$ deg and for a varying magnetic angle, respectively.

6.1 SEAD of non-prompt redeposited particles

The energy distribution of Γ_{net}, or in other words, of the non-promptly redeposited (NP) fraction, as presented in equations (29), is compared with a series of Monte Carlo results. Figures 7, 8 illustrate the two-groups model and Monte Carlo estimates of the SEAD for the NP population. In figure 7 are depicted the SEAD of the NP fraction as a function of energy and poloidal angle. Specifically, figures 7a and 7b illustrate the NP energy and angular distribution when the electron density at the sheath entrance is set to 5e18 m^{-3} while keeping other sheath parameters constant. Similarly, figures 7c and 7d portray the NP energy and angular distribution when the electron density at the sheath entrance is 5e19 m^{-3} with the remaining sheath parameters unchanged from the lower density case. In figures 7a and 7c one sees that for both electron densities, the NP energy distribution is accurately represented with the two-groups model. Conversely, figures 7b and 7d show that the NP poloidal distribution given by the two-groups model is more peaked around $\theta = 40$ deg with respect to MC results. This suggests that the two-groups model tends to provide lower estimates for the number of eroded particles found in the tail associated with large θ values.

Ultimately, figure 8 presents polar plots illustrating the azimuth distribution. The analytical azimuth distribution is discontinuous because of the way the threshold distance z^{*G} is calculated in equation (21). Specifically, z^{*G} exhibits asymmetry with respect to ϕ because of the term $[1 - 2H(\phi - \pi)]$ on the right-hand side of the same equation. The Heaviside function H causes $[1 - 2H(\phi - \pi)]$ to be equal to plus one when $\phi \in [0, \pi]$, otherwise, it is equal to minus one. As depicted in figure 8a, this discontinuous solution accurately represents the MC azimuth distribution for the case of relatively low electron density. However, as shown in figure 8b, the analytical solution deviates from the MC results when the electron density is higher. This discrepancy arises because at higher density, W has a shorter ionization mean free path, leading to more particles ionizing in the sheath and experience deviation by the drift force $\vec{E} \times \vec{B}$ towards $\phi = 3/2\pi$.

6.2 Source temperature

The NP energy distribution can be utilized to get the source temperature as shown in equation (30).

$$T_s = \frac{2}{3} \int SEAD^{NP}(E)\ E dE \tag{30}$$

It is worth reminding that equation (30) refers to the distribution of not redeposited neutrals. As a result, only if energy is conserved during the first Larmor period after ionization equation (30) will give a proper

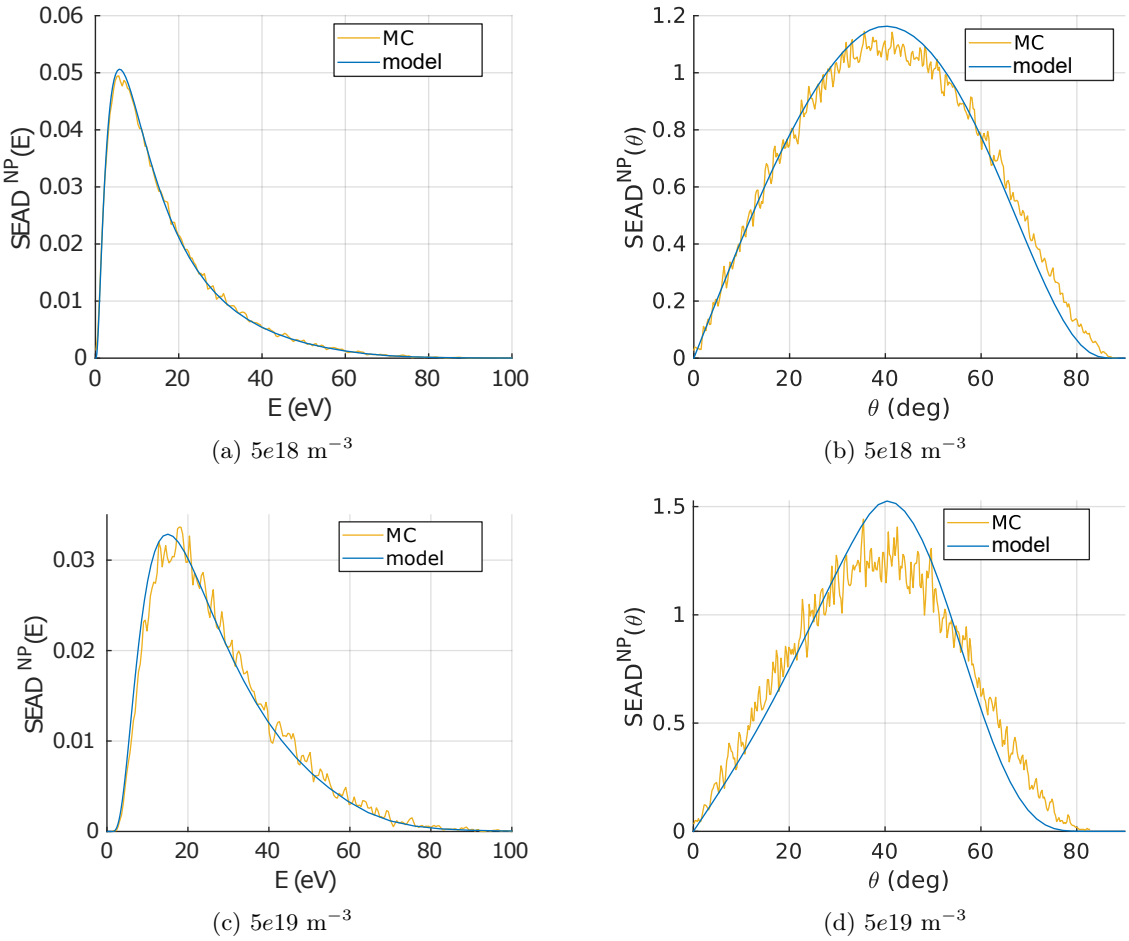

(a) $5e18$ m^{-3} (b) $5e18$ m^{-3}

(c) $5e19$ m^{-3} (d) $5e19$ m^{-3}

Figure 7: SEAD(E) and SEAD(θ) of the NP population of sputtered neutral W caused by a flux of nitrogen ions (N^{+5}), estimated with Monte Carlo (MC) and the two-groups model model for two different electron densities at the sheath entrance $n_e = 5e18$ m^{-3} and $n_e = 5e19$ m^{-3}. All other parameters are fixed: $T_e = T_i = 20$ eV, $B = 3.7$ T, and $\alpha_B = 4$ deg.

estimate of the source temperature. In figure 9, the source temperature estimates for tungsten (denoted as T_s in section 2.2) are illustrated, employing the two-groups model and Monte Carlo simulations. The variation of T_s is displayed in relation to the magnetic incidence angle α_B, considering the erosion of tungsten under the bombardment of a flux of N^{+5} ions. Notably, for grazing α_B angles the ionization length of sputtered neutrals is lower compared to larger angles, thus more particles are energetically redeposited. Indeed, the fraction f_R^E increases with α_B, see figure 4a, as well as the parameter a introduced in equation (20). Consequently, the energy of the NP population is higher. The two-groups model tends to overestimate the temperature especially in the high density case. This happens because energy is not preserved, and particles use up some of their energy to overcome the electric potential drop. One way to simulate the energy sink related to the remaining potential drop is by redefining T_s as a function of $V(\lambda_z^{*E})$, where λ_z^{*E} is the electrostatic threshold distance as defined in equation (12). The value $V(\lambda_z^{*E})$ could be used to simulate the average energy sink particles encounter during motion. A redefinition of T_s based on Monte Carlo numerical results is reported in equation (31). In figure 9, the red-dashed line shows that T_s from equation (31) better represents Monte Carlo results. Nonetheless, this approach requires further analyses.

$$T_s = \frac{2}{3}\left(\int SEAD^{NP}(E)\ EdE + \frac{2}{3}V(\lambda_z^{*E})\right) \tag{31}$$

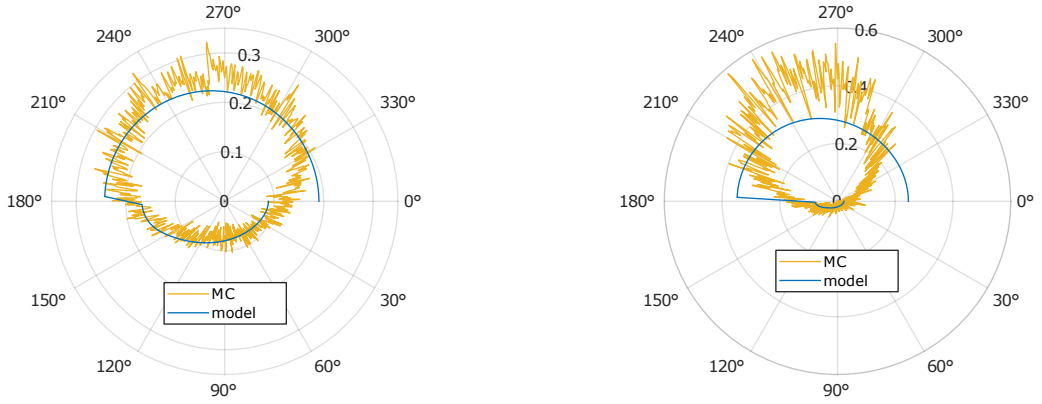

(a) 5e18 m^{-3} (b) 5e19 m^{-3}

Figure 8: SEAD(ϕ) of the NP population of sputtered neutral W caused by a flux of nitrogen ions (N^{+5}), estimated with Monte Carlo (MC) and the two-groups model model for two different electron densities at the sheath entrance $n_e = 5e18$ m^{-3} and $n_e = 5e19$ m^{-3}. All other parameters are fixed: $T_e = T_i = 20$ eV, $B = 3.7$ T, and $\alpha_B = 4$ deg.

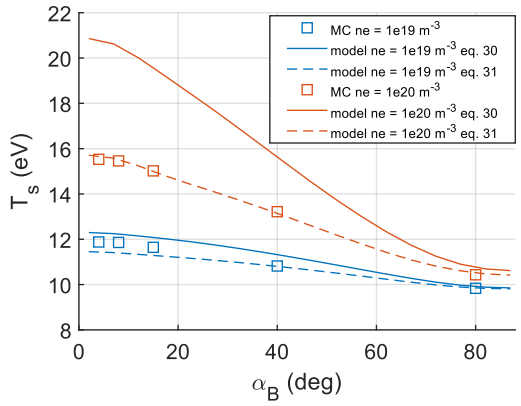

Figure 9: Temperature of non-promptly redeposited W sputtered by a flux of Nitrogen ions (N^{+5}) for two different electron densities at the sheath entrance and varying α_B. Two-groups model results are represented by the full line (equation (30)) and dashed line (equation (31)), while Monte Carlo results are depicted by squares. Other parameters were held constant: $T_e = T_i = 20$ eV, and $B = 3.7$ T.

6.3 Fluid parallel velocity

To characterize a fluid source it is also necessary to estimate its mean parallel velocity along the magnetic field. Similar to energy, this is another quantity that is conserved even after ionization, if ion-ion collisions are neglected and if the potential electric drop $V(\lambda_z^{*E})$ is small compared to their initial energy. Hence, the average parallel velocity $\overline{v_\parallel}$ can be calculated if the SEAD^{NP} of neutrals associated to the $1 - f_p$ fraction is known as illustrated in equation (32).

$$\overline{v_\parallel} = \int SEAD^{NP}(E,\theta,\phi) v_\parallel(E,\theta,\phi) dE d\theta d\phi \tag{32}$$

Figure 10 shows $\overline{v_\parallel}$ of W net flux caused by N^{+5} ions bombardment, as a function of the magnetic angle α_B, calculated with both two-groups model (equation 32) and MC simulations. Since in the given case the

magnetic field is directed towards the wall, the parallel-to-B velocity is actually negative. Two distinct trends are presented in figure 10: one for a low electron density case ($n_e = 1e19$ m^{-3}) and another for a high electron density case ($n_e = 1e20$ m^{-3}) at the sheath entrance.

The two-groups model results exhibit the same overall trends as the numerical ones. However, there is a disagreement in the high density case, related to the difference between the model and numerical SEAD^{NP} distributions, as previously demonstrated in figures 8 and 7. The disagreement is larger for the high density case since the potential drop $|V(\lambda_z^{*E})|$ particles need to overcome increases.

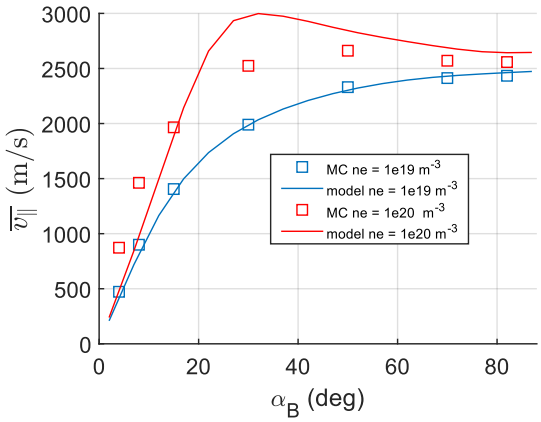

Figure 10: The average parallel velocity of W NP population due to a flux of incident nitrogen ions (N^{+5}) is examined across a range of magnetic angles α_B. The results from both Monte Carlo (MC) simulations and the two-groups model (equation (32)) are compared under two different electron densities at the sheath entrance: $n_e = 1e19$ m^{-3}, and $n_e = 1e20$ m^{-3}, in the following conditions: $B = 3.7$ T, $T_e = 20$ eV.

6.4 Scan with fixed magnetic angle

In steady-state and in the absence of collisions, the probability of redeposition depends mainly on an interplay between the ionization length along z (i.e. λ_z) of the eroded particles and the potential drop profile $V(z)$. On average, the population of eroded particles must ionize beyond the threshold distance λ_z^{*E}, see equation (12), to avoid energy-driven redeposition. At the same time, the redeposition related to gyromotion also depends on the ionization length once the magnetic angle α_B is fixed. The dimensionless parameter $\hat{\lambda}$ is proposed as the main dependent variable for the fraction of redeposited particles f_p for given α_B. The parameter $\hat{\lambda}$ is set equal to the ratio of the average ionization length along z of the sputtered population at the wall $\overline{\lambda_z}$ to the average threshold distance λ_z^{*E}. In equation (33) the formula for $\hat{\lambda}$ is reported.

$$\hat{\lambda} \equiv \frac{\overline{\lambda_z}}{\lambda_z^{*E}} \tag{33}$$

The $\hat{\lambda}$ definition of equation (33) has already been used in figure 4. Moreover, $\hat{\lambda}$ is one among other definitions of similar parameters proposed in [10], [11]. In contrast to other similar parameters, the fraction prompt $f_p(\hat{\lambda})$ follows almost a single curve regardless of the incident ion charge, hence regardless of the eroded particles high-energy tail, see figure 11.

The fraction f_p is calculated for a wide range of $\hat{\lambda}$ values in the case of W self sputtering for a given magnetic angle $\alpha_B = 4$ deg. The simulated incident ions are W^{+2} and W^{+10}. At figure 11a it is shown that the fraction $1 - f_p$ estimated by the two-groups model correlates less with $\hat{\lambda}$ than the MC output, especially for $\hat{\lambda} \lessapprox 0.7$. From figure 11b it can be seen that the two-groups model solution tends to overestimate the fraction $1 - f_p$ when $\hat{\lambda} < 1$ that is, when $\overline{\lambda_z} < \lambda_z^{*E}$. The fraction $1 - f_p$ caused by the impact of W^{+10} is overestimated by up to 5 times when $\hat{\lambda} \approx 0.5$, while for W^{+2} the ratio reaches a value of about 20 when $\hat{\lambda} \approx 0.4$. The figure 11b is enlarged to make it more readable and that is why values tending to 20 are not visible.

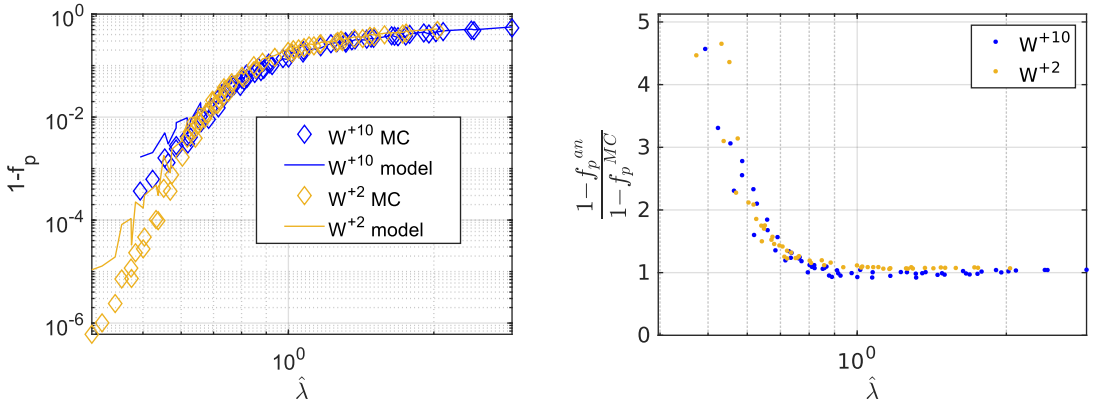

Figure 11: Ionic bombardment of W^{+2} and W^{+10} on W at a fixed magnetic angle $\alpha_B = 4$ deg. The other parameters vary, $n_e \in [5e18, 5e20]$ m^{-3}, $T_e \in [15, 30]$ eV and $B \in [2, 5]$ T.

6.5 Scan with varying magnetic angle

The prompt redeposited fraction f_p also depends on the angle α_B. In fact, as indicated in section 3.1.3, the redeposition associated with gyromotion is dependent on α_B in different ways. Both the Larmor radius and its projection onto the z-axis are functions of the angle α_B. Additionally, α_B plays a role in determining the distance covered during gyration towards or away from the wall, as expressed in equation (19). Therefore, the two-groups model assessment of f_p is tested by using α_B as a variable. Similarly to section 6.4, the case of W erosion due to self-sputtering caused by W^{+2} and W^{+10} ions is studied. In figure 12, the values of $1 - f_p$ calculated using both the two-groups model and Monte Carlo simulations are shown as a function of α_B. In figure 12a the two-groups model and numerical $1 - f_p$ trends are graphed, imposing an electron density $n_e = 1e19$ m^{-3} (low-density case). Figure 12b depicts the $1 - f_p$ ratio between the two-groups model and numerical values in the low-density case. Similarly, figures 12c and 12d illustrate the trends and ratio of $1 - f_p$ for an electron density 10 times higher ($n_e = 1e20$ m^{-3}, high-density case). For both densities, the two-groups model solution tends to overestimate the fraction $1 - f_p$, especially when $\alpha_B = 40$ degrees. For the low-density case, the maximum error reaches 12%. On the other hand, given the reduction of $\hat{\lambda}$, the high-density case reaches a maximum error of 55%.

6.6 Benchmark of f_p with previous works

The two-groups model so far has been compared with an already validated Monte Carlo code from [11]. However, it is interesting to see how the two-groups model compares to other past work, particularly in terms of the individual contributions of energetic redeposition (see section 3.1.1) or geometric redeposition (see section 3.1.2). In the work of [19], a PIC code is used to calculate the total redeposition values (denoted as f_{redep} as opposed to the prompt which is f_p) of W, both in the absence and presence of the plasma sheath, i.e., the electric field. The total redeposition provided by [19] is not directly comparable with prompt redeposition, as it includes particles that redeposit after the first Larmor period (a phenomenon called long-range redeposition in [19]). Nevertheless, the authors of [19] provide the percentages of long-range redeposited particles, allowing for the conversion from total redeposition to prompt redeposition (f_p). In addition, results are given in the absence of the plasma sheath (no electric field), so there is no energy redeposition ($f_R^E = 0$), and the results of [19] can be compared directly with the equation (23) as long as $a = 0$ and $\zeta = 1$ are fixed in equation (21). Figure 13 depicts the $1 - f_p$ values taken from the Figure 12a of [19] after being converted to prompt redeposition by eliminating the long-range redeposition shown in Figures 12b and 12c, in the same reference. The data were extracted directly from Figures 12a, 12b, and 12c of [19] using the WebPlotDigitizer v4.0 tool [20].

The comparison was conducted under identical conditions, including the incident ion W^{+12}, eroded species (W), plasma conditions at the sheath entrance (n_e^{SE}, T_e^{SE}), ionization rate coefficients (S), magnetic configura-

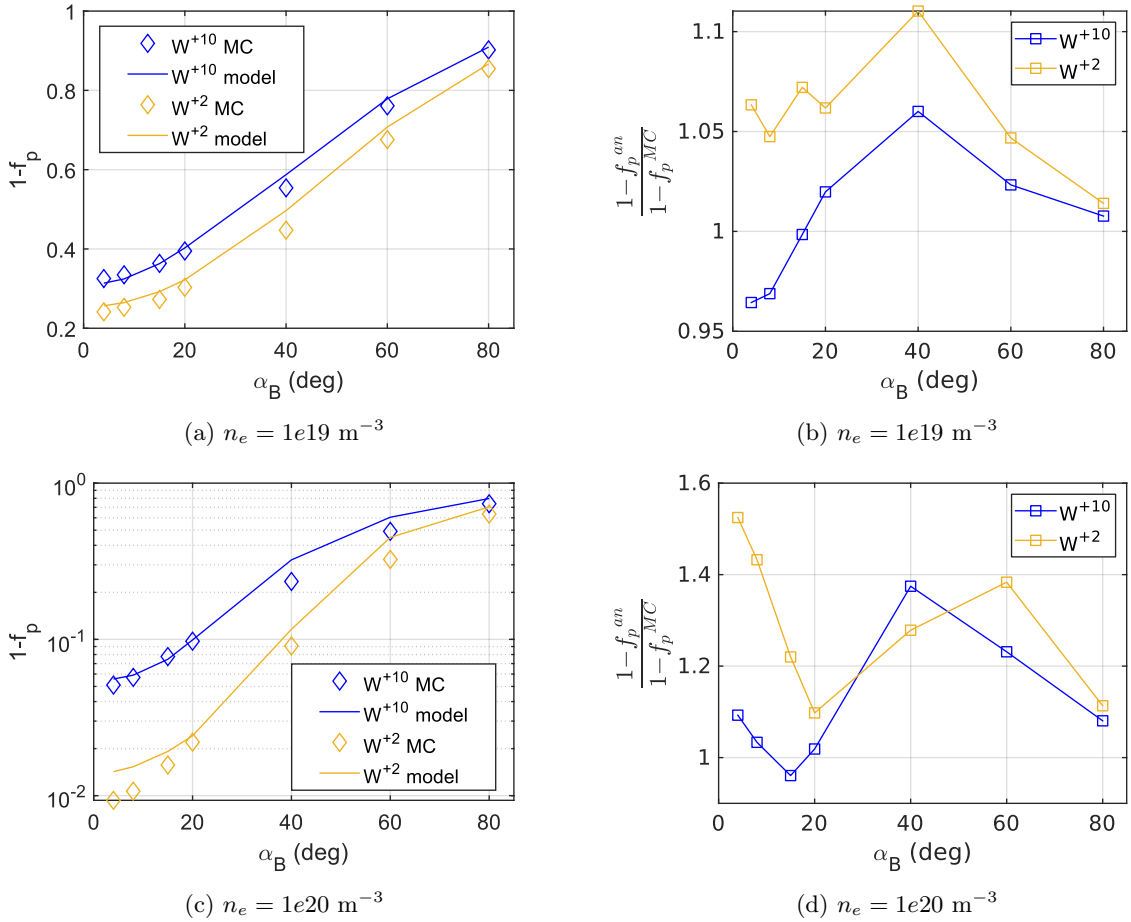

(a) $n_e = 1e19$ m^{-3}

(b) $n_e = 1e19$ m^{-3}

(c) $n_e = 1e20$ m^{-3}

(d) $n_e = 1e20$ m^{-3}

Figure 12: Ionic bombardment of W^{+2} and W^{+10} on W. A scan of $1 - f_p$ along the magnetic angle α_B is conducted using both Monte Carlo (MC) simulations and the two-groups model. The simulations are performed under fixed plasma conditions: $T_e = 20$ eV, $B = 3.7$ T, $n_e = 1e19$ m^{-3}, and $n_e = 1e20$ m^{-3}.

tion (B, α_B), SEAD model, and absence of ion-ion collisions. However, discrepancies arise in the electric field drop and the profiles of temperature and electron density. These profiles, as outlined in [19], were derived from PIC simulations. For more information regarding the input used, see figure 13. The results of the two-groups model are in agreement with those of [19], both in the presence or absence of the electric field, bringing further evidence that the code accurately reproduces prompt and geometric redeposition within its physical framework. In addition, figure 13 shows the fraction $(1 - f_p)$ according to the model of Fussman et al. [7]. It can be seen that the Fussman et al. model deviates from f_p values either in the presence or absence of the sheath.

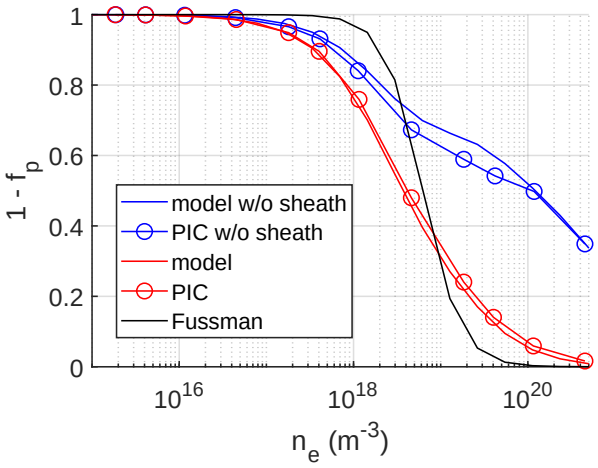

Figure 13: Ionic bombardment of W^{+12} on W: scan along electron density at sheath entrance, with fixed magnetic angle $\alpha_B = 3$ deg, temperature $T_e = T_i = 25$ eV and magnetic field intensity $B = 3$ T. Input parameters were selected to compare $1 - f_p$ values from the two-groups model with those calculated using a PIC code as described in [19]. Additionally, the analytical formula from Fussman et al. [7] is shown.

7 Conclusions

A 1D semi-analytical model, called two-groups model, is proposed to estimate prompt redeposition. This model is designed to operate under the conditions of steady-state sheath over a planar surface without ion-ion collisions. It assumes that the characteristic length of redeposition is sufficiently small, allowing the redeposition to be treated as a local phenomenon where plasma quantities vary solely in the direction perpendicular to the surface. The model theory offers new insights and physical interpretation about prompt redeposition. Additionally, it provides estimates of important quantities regarding impurity sources: net flux, average charge state, temperature and mean parallel-to-B velocity. In the two-groups model, prompt redeposition is directly related to the probability that neutrals have to redeposit given their initial energy and direction. The redeposition probability is approximated as being caused either by the electric field or by gyromotion. A set of kinetic equations to estimate the probability a neutral particle will redeposit only because of the electric field and the total gross flux fraction redepositing because of the same reasons is proposed in section 3.1.1. A model to describe the gyromotion-driven redeposition including the effects of a varying magnetic field angle, the perpendicular and parallel-to-B velocities, multiple ionization, and the returning of particles inside the sheath during their gyromotion, is advanced in section 3.1.2. Multiple ionization are addressed via an analytically solvable set of differential equations, reported in section 4. The net flux and some of its fluid quantities, such as mean parallel-to-B velocity and temperature are directly related to the Sputtered energy and Angular Distribution (SEAD) of sputtered neutrals at the wall. Such approximation based on the conservation of energy and parallel-to-B velocity is valid only in the absence of collisions, and if particles ionize on average in a volume where the potential drop is negligible compared to their initial energy. Ultimately, the formulation of the prompt redeposited fraction is treated in section 5. The two-groups model is utilized to assess the net flux of sputtered tungsten (W), its average charge, temperature and mean parallel-to-B velocity across a wide range of plasma conditions, as detailed in section 6. The two-groups model is compared with corresponding results obtained from Monte Carlo (MC) simulations, which are considered as a reference. The two-groups model and MC solutions generally agree if the ionization length of sputtered neutrals is large enough to conserve energy and parallel motion along the first gyration. Conversely, as the ionization length decreases, the two-groups model tends to underestimate the prompt-redeposited fraction because the trajectories of particles overcoming the electric field are still largely influenced by the remaining potential drop, increasing the likelihood of redeposition. Additionally, other phenomena such as $\vec{E} \times \vec{B}$ drifts, come into play. Results show that because of the electric field redepositing particles with lower energies, the source temperature T_s is larger than the temperature of W at the wall. Similarly, because of gyromotion-driven redeposition, the azimuth distribution of the net source tends to be more peaked towards $\phi \in [\pi, 3/2\pi]$. This asymmetry is further intensified by $\vec{E} \times \vec{B}$

drifts. Hypothetically, if it were possible to manipulate the initial azimuth distribution of eroded particles, directing them more towards $\phi = \pi/2$, redeposition could be significantly increased. Of course, inverting the magnetic field direction would simply mirror the azimuth distribution without enhancing prompt redeposition. In the specific conditions for which the model is designed, it serves as a rapid tool for calculating crucial quantities related to impurity sources. Moreover, the two-groups model exhibits flexibility, allowing it to operate with any SEAD at the wall, 1D electron density, and temperature profiles. Additionally, it can accept any 1D electric potential drop in the sheath, provided that it is monotonically varying. This flexibility implies that factors such as wall roughness could be considered, assuming they are small compared to the sheath width. The implementation of roughness could involve modifications to the sputtering yield functions and the SEAD. Anyway, it is important to acknowledge also the model limitations especially in the case of applying it in tokamak-scale simulations as a boundary condition tool for solving impurity transport with fluid codes. Firstly, the code is constrained by limited spatial and temporal resolution. Prompt redeposition encompasses the ionization time of neutrals and a Larmor period of the eroded species. As particles redeposit within a distance roughly equivalent to their first ionization Larmor radius ρ_L, and since plasma quantities are treated locally, in tokamak-scale simulations, plasma profiles at the sheath entrance must be averaged over a distance on the order of ρ_L. Consequently, intricate geometrical details might not be fully captured. Moreover, there will always be a fraction of particles situated at the boundaries between cells with constant plasma quantities that may traverse into other cells, emphasizing the need for proper cell dimensioning to minimize such events. Another limitation pertains to the proximity between walls along their perpendicular directions. For instance, in the case of two parallel walls, their separation must be sufficient to prevent mutual redeposition. In the future, enhancing the two-groups model could involve integrating ion-ion collisions, thermal forces, considering the influence of surface roughness and the Impact Angular Distribution (IAD) on sputtering yield and the SEAD. For instance, the model proposed in [21] offers a rapid calculation method for the IAD, which could be beneficially incorporated into the two-groups model. For now, experiments could be conducted to validate the model's assumptions of locality and the absence of ion-ion collisions. To do this, the net-to-gross flux ratio of flat surfaces could be measured by exposing material samples to plasmas. The exposed material should have a characteristic length larger than the eroded species' Larmor radius and should be positioned at an appropriate distance from other walls. Ideally, the code should be tested initially using a weakly ion-ion collisional plasma sheath for the material exposure. Additionally, the plasma electron density and temperature should be almost uniform along the plane parallel to the eroded surface. If successful, a plasma collisionality scan could be performed while maintaining uniform electron density and temperature. Regarding the hypothesis of locality, it would be interesting to check whether non-uniform radial profiles of temperature and density could be averaged over the sample to obtain acceptable results between the model and experiments. From a modeling perspective, the two-groups model should be integrated into multispecies fluid codes as a boundary tool and compared to full kinetic Monte Carlo simulations regarding tungsten (W) contamination inside the plasma core. If the model proves capable of accurately describing both experimental results and current modeling tools, it could become a viable option for rapidly assessing impurity sources in future simulations, paving the way for studies of the temporal dynamics of the feedback loop between plasma contamination, radiative power, and wall erosion.

References

[1] J. W. Coenen, "Fusion Materials Development at Forschungszentrum Jülich," en, *Advanced Engineering Materials*, vol. 22, no. 6, p. 1 901 376, Jun. 2020, ISSN: 1438-1656, 1527-2648. DOI: 10.1002/adem.201901376.

[2] V. Ostuni, J. Morales, J.-F. Artaud, *et al.*, "Core radiative collapse characterisation and integrated modelling in WEST plasmas," en, *Nuclear Fusion*, vol. 62, no. 10, p. 106 034, Sep. 2022, ISSN: 0029-5515. DOI: 10.1088/1741-4326/ac8cd6.

[3] H. Bufferand, G. Ciraolo, Y. Marandet, *et al.*, "Numerical modelling for divertor design of the WEST device with a focus on plasma–wall interactions," en, *Nuclear Fusion*, vol. 55, no. 5, p. 053 025, Apr. 2015, ISSN: 0029-5515. DOI: 10.1088/0029-5515/55/5/053025.

[4] H. Bufferand, P. Tamain, S. Baschetti, *et al.*, "Three-dimensional modelling of edge multi-component plasma taking into account realistic wall geometry," *Nuclear Materials and Energy*, vol. 18, pp. 82–86, Jan. 2019, ISSN: 2352-1791. DOI: 10.1016/j.nme.2018.11.025.

[5] S. Wiesen, D. Reiter, V. Kotov, *et al.*, "The new SOLPS-ITER code package," *Journal of Nuclear Materials*, PLASMA-SURFACE INTERACTIONS 21, vol. 463, pp. 480–484, Aug. 2015, ISSN: 0022-3115. DOI: 10.1016/j.jnucmat.2014.10.012.

[6] D. Reiter, M. Baelmans, and P. Börner, "The EIRENE and B2-EIRENE Codes," *Fusion Science and Technology*, vol. 47, no. 2, pp. 172–186, Feb. 2005, ISSN: 1536-1055. DOI: 10.13182/FST47-172.

[7] 1. International Conference on Plasma Physics and Controlled Nuclear Fusion Research (15 Sevilla), *Plasma physics and controlled nuclear fusion research 1994: proceedings of the fifteenth International Conference on Plasma Physics and Controlled Nuclear Fusion Research, held by the International Atomic Energy Agency in Seville, 26 September - 1 October 1994 : in four volumes. 3.* (Proceedings series), Anglais. Vienna: IAEA, 1996, ISBN: 978-92-0-103795-4.

[8] A. V. Chankin, D. P. Coster, and R. Dux, "Monte Carlo simulations of tungsten redeposition at the divertor target," en, *Plasma Physics and Controlled Fusion*, vol. 56, no. 2, p. 025 003, Feb. 2014, ISSN: 0741-3335, 1361-6587. DOI: 10.1088/0741-3335/56/2/025003.

[9] D. Tskhakaya and M. Groth, "Modelling of tungsten re-deposition coefficient," *Journal of Nuclear Materials*, PLASMA-SURFACE INTERACTIONS 21, vol. 463, pp. 624–628, Aug. 2015, ISSN: 0022-3115. DOI: 10.1016/j.jnucmat.2014.10.086.

[10] J. Guterl, I. Bykov, R. Ding, and P. Snyder, "On the prediction and monitoring of tungsten prompt redeposition in tokamak divertors," *Nuclear Materials and Energy*, vol. 27, p. 100 948, Jun. 2021, ISSN: 2352-1791. DOI: 10.1016/j.nme.2021.100948.

[11] L. Cappelli, N. Fedorczak, J. P. Gunn, S. D. Genova, J. Guterl, and E. Serre, "Study of the erosion and redeposition of W considering the kinetic energy distribution of incident ions through a semi-analytical model," en, *Plasma Physics and Controlled Fusion*, vol. 65, no. 9, p. 095 001, Jul. 2023, ISSN: 0741-3335. DOI: 10.1088/1361-6587/ace282.

[12] J. Romazanov, D. Borodin, A. Kirschner, *et al.*, "First ERO2.0 modeling of Be erosion and non-local transport in JET ITER-like wall," en, *Physica Scripta*, vol. 2017, no. T170, p. 014 018, Sep. 2017, ISSN: 1402-4896. DOI: 10.1088/1402-4896/aa89ca.

[13] T. R. Younkin, D. L. Green, A. B. Simpson, and B. D. Wirth, "GITR: An accelerated global scale particle tracking code for wall material erosion and redistribution in fusion relevant plasma–material interactions," *Computer Physics Communications*, vol. 264, p. 107 885, Jul. 2021, ISSN: 0010-4655. DOI: 10.1016/j.cpc.2021.107885.

[14] M. W. Thompson, "II. The energy spectrum of ejected atoms during the high energy sputtering of gold," *The Philosophical Magazine: A Journal of Theoretical Experimental and Applied Physics*, vol. 18, no. 152, pp. 377–414, Aug. 1968, ISSN: 0031-8086. DOI: 10.1080/14786436808227358.

[15] R. Behrisch and W. Eckstein, *Sputtering by Particle Bombardment: Experiments and Computer Calculations from Threshold to MeV Energies*, en. Springer Science & Business Media, Jul. 2007, ISBN: 978-3-540-44502-9.

[16] I. Borodkina, D. Borodin, A. Kirschner, *et al.*, "An Analytical Expression for the Electric Field and Particle Tracing in Modelling of Be Erosion Experiments at the JET ITER-like Wall," en, *Contributions to Plasma Physics*, vol. 56, no. 6-8, pp. 640–645, Aug. 2016, ISSN: 0863-1042, 1521-3986. DOI: 10.1002/ctpp.201610032.

[17] H. P. Summers, *The ADAS User Manual*, 2004.

[18] A. Kirschner, D. Tskhakaya, S. Brezinsek, *et al.*, "Modelling of plasma-wall interaction and impurity transport in fusion devices and prompt deposition of tungsten as application," en, *Plasma Physics and Controlled Fusion*, vol. 60, no. 1, p. 014 041, Nov. 2017, ISSN: 0741-3335. DOI: 10.1088/1361-6587/aa8dce.

[19] N. Mellet, J. P. Gunn, B. Pégourié, Y. Marandet, C. Martin, and P. Roubin, "Tungsten erosion by impurities and redeposition: Focus on the magnetised sheath," en, *Plasma Physics and Controlled Fusion*, vol. 59, no. 3, p. 035 006, Feb. 2017, ISSN: 0741-3335. DOI: 10.1088/1361-6587/aa576c.

[20] *PlotDigitizer: Version 4.0*.

[21] K. Schmid, M. Mayer, C. Adelhelm, M. Balden, S. Lindig, and t. A. U. team the, "Impact of gyromotion and sheath acceleration on the flux distribution on rough surfaces," en, *Nuclear Fusion*, vol. 50, no. 10, p. 105 004, Aug. 2010, ISSN: 0029-5515. DOI: 10.1088/0029-5515/50/10/105004.